1 **Initial observations of lunar impact melts and ejecta flows with the Mini-RF radar**
2

3 Lynn M. Carter
4 NASA Goddard Space Flight Center
5 Planetary Geodynamics Lab, Code 698
6 Greenbelt, MD 20771
7
8 Catherine D. Neish, D. B. J. Bussey,
9 The Johns Hopkins University Applied Physics Lab
10 11100 Johns Hopkins Rd.
11 Laurel, MD 20723
12
13 Paul D. Spudis,
14 Lunar and Planetary Institute
15 3600 Bay Area Blvd.
16 Houston, TX 77058
17
18 G. Wesley Patterson, Joshua T. Cahill, R. Keith Raney
19 The Johns Hopkins University Applied Physics Lab
20 11100 Johns Hopkins Rd.
21 Laurel, MD 20723
22
23

Abstract: The Mini-RF radar on the Lunar Reconnaissance Orbiter spacecraft has revealed a great variety of crater ejecta flow and impact melt deposits, some of which were not observed in prior radar imaging. The craters Tycho and Glushko have long melt flows that exhibit variations in radar backscatter and circular polarization ratio along the flow. Comparison with optical imaging reveals that these changes are caused by features commonly seen in terrestrial lava flows, such as rafted plates, pressure ridges, and ponding. Small (<20 km) sized craters also show a large variety of features, including melt flows and ponds. Two craters have flow features that may be ejecta flows caused by entrained debris flowing across the surface rather than by melted rock. The circular polarization ratios (CPRs) of the impact melt flows are typically very high; even ponded areas have CPR values between 0.7-1.0. This high CPR suggests that deposits that appear smooth in optical imagery may be rough at centimeter- and decimeter- scales. In some places, ponds and flows are visible with no easily discernable source crater. These melt deposits may have come from oblique impacts that are capable of ejecting melted material farther downrange. They may also be associated with older, nearby craters that no longer have a radar-bright proximal ejecta blanket. The observed morphology of the lunar crater flows has implications for similar features observed on Venus. In particular, changes in backscatter along many of the ejecta flows are probably caused by features typical of lava flows.

1. Introduction

The impact process generates substantial melted material that is deposited in and around the crater. Early observations of the Moon revealed melt features associated with fresh impact craters; these features included thin veneers, ponds, and flows [*Shoemaker et al.,* 1968; Guest, 1973; *Howard and Wilshire*, 1975; *Hawke and Head*, 1977]. *Hawke and Head* [1977] found that the types and distribution of melt associated with impacts varies with crater size; craters with diameters less than 10 km were observed to have mostly veneers and small ponds on and outside the rims, while larger 20-50 km diameter craters are more likely to have significant melt flows. Ponds and melt flows can be found up to two crater radii from the rim of lunar craters, and the largest craters (above 50 km diameter) were observed to have ponds, but no flows [*Hawke and Head* 1977].

Magellan radar images of Venus also revealed long impact crater ejecta flows with complex radar backscatter variations that extend up to 14 crater radii from the rims [*Phillips et al.* 1991; *Chadwick and Schaber* 1993; *Asimov and Wood* 1992]. The transitions between radar bright and radar dark backscatter within a given flow have been attributed to various types of surface roughness changes, including differences in entrained clast abundance along the flow [*Chadwick and Schaber* 1993], deposition of rough, blocky material caused by topographic obstruction of a transient impact-induced hot vapor cloud [*Schultz* 1992], or changes in lava-like flow features that form in flowing impact melt [*Johnson and Baker*, 1994].

There are also multiple models for ejecta flow formation, which fall into two major categories. The first group of models suggests that the flows are caused by hot, turbulent density currents similar to pyroclastic flows that entrain melt, vapor and debris [*Shoemaker et*

65   *al.* 1986; *Phillips et al.* 1991; *Schultz et al.* 1992]. This flow emplacement mechanism is

66   sometimes suggested to be an early stage process, particularly because proximal crater ejecta

67   blanket materials often appear to overlie flow features on Venus [*Asimov and Wood* 1992]. In

68   this case, crater ejecta may have flow-like boundaries that are produced primarily by

69   deposition of solid debris rather than by flowing melted rock.

70   A second hypothesis suggests that, subsequent to ejecta emplacement, melted rock

71   undergoes late-stage segregation and then travels over the surface like a lava flow [*Shoemaker*

72   *et al.* 1968; *Phillips et al.* 1991; *Asimov and Wood* 1992; *Johnson and Baker* 1994]. In this

73   case, the flow boundaries are created by the impact melt, which likely entrains both country

74   rock and ejecta clasts as it flows over and around the previously emplaced ejecta. For the

75   Venus craters, it is possible that both processes (debris-rich flows and flowing impact melt)

76   can occur and this leads to the variety of different flow morphologies seen in radar images.

77   The prevalence and length of the ejecta flows on Venus are likely due to a combination of

78   factors, including the high surface temperatures, high mean impact velocities, and high

79   atmospheric pressure [*Phillips et al.* 1991; *Asimov and Wood* 1992].

80   There are multiple physical parameters that influence the emplacement of melted rock

81   during and after impacts. The angle of impact controls the direction of ejected material and

82   can lead to increased deposition of melt downrange and to the sides of the impact site [*Schultz*

83   1996; *Pierazzo and Melosh* 2000]. Impact angle is often cited as one of the primary

84   contributors to large amounts of melt deposition outside the crater [*Hawke and Head* 1977;

85   *Phillips et al.* 1991]. Melt flows will contain some component of unmelted country rock clasts

86   produced by the impact event, of which increasing amounts will increase the viscosity of the

87   flow. Topographic gradients can allow melt to escape from the crater walls, speed or slow the

88   flow as it travels across the surface, or trap melt material in topographic lows to form ponds

89   [*Hawke and Head* 1977; *Johnson and Baker* 1994]. Recent images from the Lunar

90   Reconnaissance Orbiter Camera (LROC) Narrow Angle Camera (NAC) have shown a

91   complex evolution of melt flows, including multiple-stage melt injection, flow inflation,

92   erosion of crater walls and uphill movement of melt [*Bray et al.* 2010]. These processes

93   suggest that the formation of melt flow features may vary extensively depending on the

94   impact conditions, and may have relatively long cooling times [*Bray et al.* 2010].

95   Radar observations of the lunar melt flows can provide additional information beyond

96   what can be learned with optical imaging. Radar is sensitive to roughness on the scale of the

97   radar wavelength, and at S-band wavelengths (12.6 cm), it can be used to assess surface and

98   sub-surface roughness of the centimeter to decimeter scale. This is somewhat smaller than

99   what is directly visible in high-resolution imaging, including the LROC NAC, which has a 50

100 cm/pixel resolution [*Robinson et al.* 2010]. For typical lunar regolith dielectric properties

101 [*Carrier et al.* 1991], the 12.6 cm wavelength Mini-RF radar wave can penetrate up to ~1 m

102 below the surface. This allows detection of buried impact melt and associated flow structures

103 that have been smoothed over by regolith deposition and maturation and are consequently no

104 longer visible in optical images (e.g. *Campbell et al.* [2010]).

105   Prior radar observations of lunar impact craters using Arecibo Observatory S-band

106 (12.6 cm wavelength) radar system and the Green Bank Telescope have revealed rough, radar

107 bright flows that can extend greater than two crater radii from the rim [*Campbell et al.* 2010].

108 Some of these flows had not been previously identified in imaging data (e.g. Aristillus)

109 [*Campbell et al.* 2010]. The melt flows have very high values of the radar circular polarization

110 ratio, which suggests that the flow surfaces have roughness characteristics greater than

111 terrestrial a'a lavas [*Campbell et al.* 2010]. The Mini-RF radar on LRO can likewise be used

112 to assess melt flow roughness, to determine whether there is structure internal to the flow, and

113 to map flow boundaries, all of which can lead to a better understanding of how impact melt

114 and debris flows are emplaced. Mini-RF has a somewhat higher resolution (15x30 m/pixel)

115 than the highest resolution ground-based radar data (20-30 m/pixel) [*Raney et al.* 2011;

116 *Campbell et al.* 2010]. Mini-RF can also image the lunar farside and the lunar poles to search

117 for examples of impact melts not previously observed by radar.

118

119 **2. Mini-RF Polarimetric Data**

120

121   The Mini-RF instrument on the LRO has acquired S-band (12.6 cm wavelength) radar

122 imagery of many impact craters at a resolution of 15x30 m [*Raney et al.* 2011]. The radar

123 transmits a circular-polarized wave and measures two orthogonal received polarizations

124 (horizontal, H and vertical, V). These data can be used to generate images for each element of

125 the Stokes vector (*Jackson* [1999]; *Green* [1968]):

126
$$S = \begin{bmatrix} S_1 \\ S_2 \\ S_3 \\ S_4 \end{bmatrix} = \begin{bmatrix} \left\langle |E_H|^2 \right\rangle + \left\langle |E_V|^2 \right\rangle \\ \left\langle |E_H|^2 \right\rangle - \left\langle |E_V|^2 \right\rangle \\ 2\mathrm{Re}\left\langle E_H E_V^* \right\rangle \\ -2\mathrm{Im}\left\langle E_H E_V^* \right\rangle \end{bmatrix} \qquad (1)$$

127

128   The first Stokes parameter image (S_1) is a measure of the total average power of the

129 echo. The S_2 and S_3 Stokes parameter images measure the linearly polarized power, and the

130 S_4 Stokes parameter image provides information on the magnitude of the circularly polarized

131 power and whether it is right or left circular-polarized. These four polarization images are a

132   primary data product of Mini-RF, and are mapped to the lunar coordinate grid with a

133   resolution of 15 m/pixel. The center-swath incidence angle for flat surfaces varies from ~48-

134   55°. Changes in surface topography lead to a large range of incidence angles in many images,

135   particularly images in highland terrains.

136   The circular polarization ratio (CPR) can be used as an indicator of surface roughness.

137   The CPR, which is the ratio of the same-sense circular polarization as was transmitted to the

138   opposite-sense circular polarization as was transmitted, can be calculated from [*Stacy*, 1993]:

139

140    $$CPR = \frac{S_1 - S_4}{S_1 + S_4} \qquad\qquad (2)$$

141

142   Surfaces that are very smooth at wavelength scales will lead to low CPR values (<0.4),

143   while scattering from surfaces that are rough at the wavelength scale, and have double-bounce

144   geometries, lead to moderate to high (0.4-1.0) CPR values. A double-bounce geometry occurs

145   when the radar wave reflects from two surfaces before returning to the receiver, thereby

146   causing the received circular polarization state to be the same as that transmitted. Extremely

147   rugged terrain can sometimes produce circular polarization ratios greater than one (e.g.

148   *Campbell and Campbell* [1992]; *Campbell* [2009]). These high CPR values cannot be caused

149   by Bragg scattering from wavelength scale roughness (e.g *Ulaby et al.* [1996]) and require

150   that a significant amount of the backscatter come from double-bounce geometries. For

151   terrestrial analog surfaces, CPR values near or above one correspond to surfaces that have a

152   rugged appearance and are rough at centimeter to meter, and sometimes decimeter, scales

153   (e.g. Campbell and Campbell [1992]).

154   The circular polarization ratio also changes with incidence angle (lunar examples can

155   be found in *Campbell et al.* [2010], *Carter et al.* [2010], *Carter et al.* [2009]), because at low

156   (nadir) incidence angles, the backscatter is dominated by mirror-like quasi-specular scattering.

157   Therefore, we compare CPR values for surfaces that were observed at similar incidence

158   angles. For this paper, the CPR images were derived by averaging the S1 and S4 images to a

159   resolution of 60 m/pixel and then forming the CPR. This extra averaging reduces the radar

160   speckle noise and therefore improves the visibility of some polarization features.

161   The Mini-RF data sometimes have a gradient in the circular polarization ratio across

162   the range (or horizontal) dimension of the image and the circular polarization values given in

163   this paper have uncertainties related to this issue. Gradients as large as 0.3 have been

164   measured for a few images, but gradients between 0.1 and 0.2 are more common. These

165   values exceed the change in CPR that could be caused by the few degree incidence angle

166   change across the swath width (range dimension). Prior measurements of the lunar surface at

167   the Mini-RF wavelength (S-band) show that CPR changes by only a few tenths as the

168   incidence angle changes by ~5° [*Campbell et al.* 2010; *Carter et al.* 2009]. For two craters

169   discussed in this paper (Glushko, Aristillus), Mini-RF data was acquired at a similar incidence

170   angle to published ground-based radar data and can be directly compared. In these cases, the

171   CPR values are within 0.05 of those reported in *Campbell et al.* [2010], which suggests that

172   the CPR values measured by Mini-RF are consistent with prior data.

173   However, for lunar farside craters, there is no alternative data source to check the

174   calibration. In an attempt to mitigate these issues, we have not used CPR measurements in

175   cases where the gradient is particularly bad (e.g. more than +0.1 across the image). Most of

176   the images used in this paper have a CPR gradient less than ~0.05. Because of the general

177   match to ground-based data for the nearside cases, for the low- to moderate-gradient cases

178 used here, we estimate that the systematic errors are no more than ±0.1. Below, we focus on

179 comparing CPR values that are very high (greater than 1), high (0.7-1.0) and moderate (0.6-

180 0.7), to avoid the need for precise CPR numbers. Additional calibration is currently ongoing

181 to improve the quantitative polarimetry from Mini-RF.

182

183 **3. Surface Properties of Melt Flows**

184   Mini-RF has mapped ~66% of the lunar surface at mean incidence angles (on flat

185 terrain) between ~48°-54°, and has imaged many impact craters with ejecta flows and melt

186 ponds. Below, we discuss the surface properties of some of these flow features for craters

187 with different size ranges. The size divisions were chosen to roughly correspond to those used

188 by *Hawke and Head* [1977], who found that the importance of melt flows relative to ponds

189 and veneers varied partially based on impact crater size. The craters discussed here were

190 chosen on the basis of a survey of initial Mini-RF data and are not a statistical sample. In

191 particular, larger melt flows are easier to detect and it is possible that a systematic search of

192 the data will reveal additional small and medium sized craters with impact melt ponds and

193 ejecta flows.

194

195 *3.1 Large (50+ km diameter) impact craters*

196   Impact flows associated with large (>50 km diameter) impact craters display a wide

197 range of morphologies, including ponds and large flows. Melt flows of some craters within

198 this size range can display significant variation in radar backscatter along the flow, and can

199 look similar to radar images of impact crater flows on Venus [*Phillips et al.* 1991; *Chadwick*

200 *and Schaber* 1993]. The 85 km diameter crater Tycho (43.3° S, 248.8° E) is one example

201 [*Shoemaker et al.* 1968]. Although Tycho is visible in Earth-based radar images, the thin

202 flows are hard to detect in lower resolution Earth-based radar images.

203   Mini-RF data of flows east of Tycho reveal both dark and bright sections of the melt

204 flow that correspond to smooth and rough surfaces as seen in optical imagery (Figures 1 and

205 2). The bright areas of the flows typically have high CPR values (1.0-1.2). Radar dark parts of

206 the flow can be difficult to distinguish from the surroundings, particularly since the

207 mountainous terrain leads to a varying radar viewing geometry. However, even the radar-dark

208 portions of the flow have fairly high CPR values, often in the range of 0.8 to 0.9. The lowest

209 CPR values measured for very small parts of the smoothest melt ponds, away from any fresh

210 impact craters or the rough edges of the ponds, are between 0.6 and 0.7. These values are still

211 higher than what is measured for the non-melt flat surfaces in the area (CPR~0.55), and is

212 higher than CPR values measured for most terrestrial a'a flows [*Campbell and Campbell*

213 1992].

214   High-resolution LROC NAC images of the upper stages of the flows (Figures 2a and

215 2b) show the differences in surface texture between smooth ponded melt material and rough

216 flows. The high-CPR areas correspond to a rugged surface that looks similar to upturned

217 platey pahoehoe or a'a flows (Figure 2a). The highest CPR values in this area of the flow are

218 above 1.0, but are obscured by shadow in the LROC image. The CPR values in the non-

219 shadowed rough regions of the LROC image are between 0.9 and 1.0, which is perhaps not

220 surprising given the rugged surface. Nearby smooth areas have small craters, cooling

221 fractures, and large angular blocks. These regions have CPR values of 0.7-0.8, which are still

222 higher than the values measured for most terrestrial lava flows [*Campbell and Campbell*

223 1992], despite a fairly smooth appearance.

224   There are a couple of possible explanations for the high CPR values in areas that

225   appear smooth in optical images; either the radar pixels nearly always incorporate enough

226   rough features such as craters, fractures, or blocky regolith to create a high CPR, or the flow

227   surface is very rough at the centimeter scale, possibly due to entrained clasts or to a rugged

228   textured surface that is partially obscured by a coating of regolith. Fractured ponded lava and

229   pahoehoe flows on Earth have CPR values that are lower than a'a lava [*Campbell and*

230   *Campbell* 1992], so an additional roughness component beyond cooling cracks is likely

231   present. The fact that even very small smooth areas of the melt flow have CPRs that are

232   slightly above the average CPR value in the Tycho extended ejecta blanket suggests that there

233   is a component of centimeter scale surface or near-surface roughness not apparent in current

234   imagery.

235   The Surveyor 7 spacecraft landed near the rim of Tycho and obtained surface

236   photographs that reveal a complex near-rim geology. The area near the landing site has

237   multiple types of flow-like features that have been attributed to movement of hot gas, debris

238   and melt [*Shoemaker et al.* 1968]. These flows do not have lava-like surface flow features like

239   those seen in the eastern impact melt flows (Figure 2), but the surfaces of the Surveyor 7

240   flows are still very rough and exhibit varying degrees of cratering, likely from self-secondary

241   impacts [*Shoemaker et al.* 1968]. There are also many fields of angular blocks that are

242   probably fall-back ejecta that was deposited during the later stages of the impact process

243   [*Shoemaker et al.* 1968]. In addition to the rough lava-like flow features apparent in LROC

244   images (Figure 2), secondary cratering of the impact melt and breccia fall-back deposits

245   almost certainly contribute to the high CPR values seen in Figure 1.

246   The radar-bright parts of the Tycho melt flow have a very disrupted surface structure,

247   but in some cases, larger structural trends are present. The flow drains to the southeast,

248   funneling through terrain gaps. It narrows into a thin, channelized flow (with an overprinted

249   crater) before forming a distinct, oblong pond. Within the pond, the Kaguya Terrain Camera

250   images (Figure 2c) show a series of arcuate ridges perpendicular to the flow direction, and a

251   curving boundary that separates the rougher parts of the flow from smoother ponded material.

252   This ridged area is radar bright with high CPR values. These ridges are similar to pressure

253   ridges seen in terrestrial lava flows, which occur when hot, low-viscosity material moves

254   under a partially cooled, higher viscosity surface [*Fink and Fletcher* 1978; *Theilig and*

255   *Greeley* 1986]. In this case, the flow boundary in the middle of the pond (marked with arrows

256   in Figure 2c) may represent the boundaries of a late-stage melt movement into the pond.

257   Alternately, the smooth parts of the pond may have been created by a breakout of melt from

258   an initial rough flow that subsequently filled in the area to the south.

259   The surface texture of the pond suggests a complex formation process that may have

260   included multiple influxes of melt that pushed into the pond, and created rough terrain or

261   breakouts, after the flow had partially cooled. Different flow structures are present to the

262   north, where the Mini-RF data show sinuous radar-bright, high-CPR paths that track rougher

263   terrain along the flow direction or at flow terminal areas. These include one area where rafted

264   plates of melt were transported downstream (Figure 2b).

265   The longest flows observed to date are associated with the 55 km diameter crater

266   Aristillus (33.9° N, 1.2° E) [*Campbell et al.* 2010]. These flows are long, thin, and extend

267   over 2 crater radii from the rim [*Campbell et al.* 2010]. In contrast to Tycho, there is little

268   change in backscatter cross-section along the flow and no evidence of channeling. In addition

269   to these long flows, small ponds occur close to the crater rim, and are visible in both optical

270   and radar data. In Mini-RF data, the margins of the long flows have a complex shape that was

271   generated as the melt flowed around multiple topographic obstacles (Figure 3). Most of the

272   radar bright areas are connected, suggesting that the melt was mostly deposited as a

273   topography-constrained flow rather than as individual ponds, although some of the radar

274   bright areas do not have any apparent connection to the main flow. Similar thin melt flows on

275   Venus appear to be caused when melt flows along thin valleys or fractures [*Asimov and Wood*

276   1992; *Chadwick and Schaber* 1993]. The high radar backscatter of the melt deposits suggests

277   that their surface is very rough. The CPR values of the melts are around 0.65 (Figure 3c),

278   which is higher than those of the surrounding terrain, but lower than those of the Tycho melt

279   flows, probably because Aristillus at ~2.1 Ga [*Ryder et al.,* 1991] is significantly older than

280   Tycho (~100 Ma; *Arvidson et al.* [1976]).

281   The melt flow is barely visible in optical images and looks very similar to surrounding

282   mare basalts. Images acquired with the Kaguya Terrain Camera (10 m/pixel resolution)

283   (Figure 3d) do not show flow features within the radar bright areas, suggesting that the flows

284   are covered by a thin regolith layer. Given the penetration depth of the radar, the surface

285   covering is likely less than a meter. This mantling layer could also explain the lower CPR

286   values, since the radar backscatter would include contributions from both the surface regolith

287   and subsurface rough melt deposit. Because the flow is buried under a greater amount of

288   material than the Tycho melt flow, it is possible that there are smooth parts of the melt flow

289   that are not visible in the radar data; such areas may link some of the distal deposits that

290   appear unconnected in the radar data. Alternatively, some of the unconnected sections of the

291   flow could be ponds that formed when ballistically ejected melt was trapped in depressions.

292   The fresh crater Jackson (71 km diameter) on the far side of the Moon is similar in

293   size to Tycho and also has a large ray system. Radar images to the east of the crater show

294   features with a flow-like morphology that are significantly different from the impact melt

295   flows described above. Figure 4a is a LROC Wide Angle Camera (WAC) mosaic image of

296   the area, and Figure 4b shows the Mini-RF total power images on a WAC background with

297   the flow features marked with arrows. The circular polarization ratio images are shown in

298   Figures 4c and 4d. In this case, it looks like material has flowed around and over a series of

299   crater walls (arrows in Figure 4).

300   The flows have moderate backscatter in the central areas, but are sometimes brighter

301   at the margins and in places where the flows have a contact with an abrupt topographic

302   change (Figure 4b). The lack of radar-bright backscatter from the central regions suggests that

303   the flows are not as rugged as some parts of the melt flows observed at Tycho and Aristillus.

304   The circular polarization ratio values of the flows are higher than surrounding terrain in some

305   areas, but in other places the flows have CPR values that are very similar to the Jackson distal

306   ejecta (Figures 4c and d). The flows do not show a distinct high-CPR contrast with their

307   surroundings like the melt flows at Tycho and Aristillus, which suggests that the Jackson flow

308   features may be composed primarily of blocky ejecta. The radar bright flow edges may be

309   caused by rough deposits or by higher topography at the edges of the flow. Since there is no

310   evidence for flowing melted or ponded rock in either radar or optical images, the Jackson

311   flow features may have been caused by debris flows that entrained dust, rock, and small

312   amounts of melt and deposited material at topographic boundaries. These flows may be more

313   similar to some of the debris-rich flows observed in Surveyor 7 images of Tycho than they are

314   to the Tycho melt flows [*Shoemaker et al.* 1968].

315

3.2 Medium-sized craters (20-50 km diameter)

Prior imaging analyses have shown that craters in this size range often have significant amounts of melt material that can flow large distances from the source crater [*Hawke and Head* 1977]. The 43 km diameter crater Glushko (a.k.a. Olbers A; 8° N, 282.4° E) is a good example. Glushko has a complex melt flow pattern similar to that observed at Tycho (Figure 5). LROC Narrow Angle Camera (NAC) images show pressure ridges similar to those seen at Tycho (Figure 5c), but there do not appear to be areas of overturned and rafted plates. Radar-dark areas within the melt flow correspond to cratered ponded areas with fractures. In optical images, the surface of the flow is smoother and the flow features are less pronounced than they are for the Tycho flow, suggesting that the surface may be covered by a thicker layer of regolith.

The 26 km diameter crater Gerasimovich D (22.3° S, 238.4° E) also has significant melt deposits, despite not having a radar bright proximal ejecta blanket. A radar-bright impact melt flow extends ~2 crater radii from the rim (Figure 6). The melt flow is barely visible in LROC WAC optical images but has a subdued appearance probably caused by regolith cover (Figure 6a). The flow has a fairly uniform radar brightness compared to the Tycho and Glushko melt flows (Figure 6b), but minor variations are still present. These may be caused by slight differences in the surface texture of the buried flow, or possibly due to smoothing by varying amounts of surface coating. The CPR values are high (0.75), as they are for other radar-bright melt flows.

Another example is the well-known crater Wiener F (47 km diameter; 41.2° N, 150° E), which has both a melt flow and a ponded deposit (Figure 7). Radar images show that the

338   pomd is bright with an average CPR value of 0.98. The melt pond surface is rough and

339   ridged, similar to parts of Tycho and Glushko (Figure 7a). A bright flow feature is visible on

340   the pre-existing crater wall that faces towards the impact site. Lunar Orbiter images have a

341   favorable lighting geometry that show a ridge of material corresponding to the radar features.

342   The radar-bright flow on the wall may be either a melt flow that traveled up the wall, a blocky

343   debris flow that was pushed up the wall, or a melt veneer in which the mobile melt drained

344   back into the crater, leaving a lag deposit of unmelted clasts. The rough surface and flow

345   features present on the melt pond surface suggest that the melt was not tightly constrained

346   within the topographic boundaries of the preexisting crater, so it was able to flow and develop

347   complex surface features that were frozen in place as it cooled.

348

349   *3.3 Small craters (<20 km diameter)*

350   *Hawke and Head* [1977] observed that large amounts of impact melt first begin to be

351   seen surrounding craters between 10 and 20 km diameter. Mini-RF images of craters within

352   this size range reveal mostly radar bright ponds, veneers, and small flows.

353   A small, 13.5 km diameter unnamed rayed crater at 30.9° S, 145.5° E (south of Pavlov

354   G) has melt deposits close to its rim. Mini-RF images show a small, radar-bright flow and

355   pond extending ~1 crater radii away from the rim (Figure 8). Like many of the ponds

356   associated with larger craters, the circular polarization values are high and well matched to

357   those of the surrounding ejecta blanket. There are no radar backscatter changes within the

358   melt, suggesting a small amount of melt that cooled quickly.

359   Another unnamed 13 km diameter crater at (35.7° N, 166.0° E, west of Hutton)

360   appears to have a radar flow or bright ejecta extending from the western edge of the crater rim

361 (Figure 9). The bright melt has an unusual dark lane extending from the rim to the base of the

362 melt. The dark lane has rounded edges and a small offshoot that could indicate that it was

363 caused by some type of flow. Kaguya Terrain Camera imagery (Figure 9c) does not show any

364 obvious explanation for the difference in radar backscatter. The circular polarization ratio

365 image (Figure 9b) shows that the radar-bright ejecta has a high circular polarization ratio,

366 which is consistent with a rough surface of proximal ejecta or melt. The radar-dark lane,

367 however, has a very low CPR, which suggests scattering from terrain that has fewer rocks and

368 more fine material than the surrounding regions. The dark lane may be the result of a

369 landslide or small debris flow from the steep crater rim that left a coating of fine-grained

370 material or removed large blocks. Alternatively, the radar-dark feature may be fine-grained

371 material deposited as part of the impact process.

372   In another case, possible ejecta flow features are associated with a small, fresh 5 km

373 diameter crater to the northeast of Maunder, in the Orientale basin (Figure 10). In this case, a

374 radar bright deposit appears to have moved downhill to the south and around the topographic

375 contours of Maunder. The radar-bright feature extends ~12 crater radii from the rim. This is a

376 relatively long distance for such a small crater, although there is also a significant downhill

377 slope into Orientale basin in this area. The radar-bright areas do not have flow features (e.g.

378 pressure ridges or channels) associated with them (Figure 10c), and they are optically bright

379 and appear to lie in topographic depressions. Because the distal crater ejecta extends almost as

380 far as the radar-bright feature (10 crater radii in this area), all of the radar-bright areas along

381 the edge of Maunder crater may be rough ejecta from the impact, rather than a melt flow.

382   To the northwest, there are surface ripples extending out to 6 crater radii, and the

383 bright distal ejecta continue even farther, out to about 9 crater radii. The radar image shows

384   flow features on the side of a low hill that faces away from the impact site (Fig. 10a). This

385   feature is darker than most of the crater ejecta in the radar images, and optical images from

386   the Kaguya Terrain Camera show that it is bright, slightly raised terrain (Figure 10b). The

387   CPR values across the flow features are similar to those of the surrounding hills. This may be

388   part of a debris flow from the impact that flowed across the low hills, similar to what is seen

389   at Jackson.

390

391   *3.4 Melt deposits with ambiguous sources*

392   Two areas appear to have flows and ponds of impact melt that do not have a clear

393   source. One such example is the western side of Keeler crater (11° S, 157° E), where the radar

394   images reveal bright ponds and flows (Figure 11, 12). Some, but not all, of the melt features

395   are visible in Kaguya Terrain Camera images (Figure 11b, 12). The radar bright ponds have

396   CPR values (~0.7) much higher than the surrounding terrain (~0.3) and similar to those

397   measured for other melt deposits, suggesting that the features are impact melt related and not

398   smooth, block-poor deposits of fine-grained dust. Another similar area at around 41° N and

399   166° E was identified by *Robinson et al.* [2011] and has similar radar properties, including

400   radar bright ponds and flow features (Figure 13). The ponds are more distinct at this site, and

401   have significantly higher CPR values, possibly because they are less regolith-covered than the

402   Keeler flows and ponds. The high-resolution NAC frames of these features show abundant

403   surface texturing and block fields, consistent with high radar backscatter [Robinson et al.,

404   2011].

405   Unlike the other flows and ponds discussed in prior sections, these features are not

406   clearly associated with the rim or ejecta blanket of a specific crater. Instead, melt appears to

407 have flowed downhill into many topographic lows covering a broad area. One possible

408 explanation is that the melts were produced by oblique impacts that deposit a significant

409 amount of melted material downrange, or to the sides of, the impact site. Similar features exist

410 on Venus; for example, at Graham crater (1° N, 6° E), where some material is trapped in

411 small ponds on a hill [*Schultz* 1992]. However, oblique impacts on the smooth Venus plains

412 also generate significant flow features, in part because of the higher temperatures and higher

413 mean impact velocities that produce a larger amount of melt, and in part because the terrain is

414 often not rugged enough to trap the melt in many small ponds.

415   Identifying a source crater for the extensive melt deposits is difficult in the heavily

416 cratered highlands. For example, the Keeler site has a young impact crater (Ventris M) to the

417 north with a ray system that is noticeably symmetric, although the crater rim is slightly

418 elliptical. However, the crater is ~120 km distant, and there is no evidence for extensive melt

419 deposits near the crater itself. Another nearby oblique impact crater is Keeler V, but in this

420 case, some of the impact melt clearly flows over the rim and into the Keeler V floor (Figure

421 11d), which suggests a different source. Keeler V is also older and more degraded than other

422 nearby craters, so it is unlikely to have retained clear melt deposits. The source crater may

423 also have been a nearby, less oblique impact that did not produce a crater rim that deviates

424 from circular. The 37 km diameter crater Plante′, inside Keeler crater, has impact melt flows

425 extending from the proximal ejecta blanket, but is also over 100 km distant. The crater Keeler

426 S is the closest crater to the site. It does not have a radar bright ejecta blanket or evidence of

427 near-rim melt deposits, but neither does Gerasimovich D, which has a large melt flow.

428 Regardless of the source, these isolated melt deposits are interesting in that they suggest that

429 impact melts may cover substantial areas even in heavily cratered terrains and may remain

430 visible even as the source crater proximal ejecta ages and weathers to blend into the

431 surrounding terrain.

432

433 **4. Discussion**

434

435   The radar data described above can be used to assess the surface roughness of the

436 lunar impact melts compared to terrestrial lava flows. Many of the melt flows have a very

437 uniform, radar bright appearance, as reported by *Campbell et al.* [2010]. However, in some

438 cases, the flow changes both in backscatter and circular polarization ratio along the flow.

439 Terrestrial a'a flows have CPRs between 0.3 and 0.6 at incidence angles of 40-50 [*Campbell*

440 *and Campbell* 1992]. Blocky lava flows like SP Flow (north of Flagstaff, Arizona) have CPRs

441 of 0.8-1.2 at the same incidence angles, at 24 cm wavelength [*Campbell and Campbell* 1992].

442 At shorter wavelengths, the flows have somewhat higher CPR values. The CPR values of the

443 radar bright lunar melt flows are often greater than those of terrestrial a'a flows and similar to

444 those of blocky lava flows like SP Flow, which suggests that the flows have extremely rugged

445 surfaces at centimeter to meter scales. In cases where the CPR values of the bright flows are

446 somewhat lower in some of the older craters (e.g. Aristillus, Gerasimovich D) the melt flows

447 appear partially buried in optical images, which likely reduces the CPR. Ponded deposits that

448 appear smooth in optical data still have CPR values as great as terrestrial a'a flows [*Campbell*

449 *and Campbell* 1992], probably due to a combination of initial rough surface texture

450 subsequently filled in by dust, fallback breccia deposited on the surface, the presence of small

451 impact craters and related blocky ejecta, surface cooling fractures, and embedded county rock

452 clasts.

453   So far, within the resolution limit of the Mini-RF radar, there are no examples of small

454   craters (<20 km) with complex flows showing significant backscatter and circular polarization

455   ratio variations along the flow. The impact melt deposits of small craters are always radar-

456   bright with high CPR values. The surfaces of many of the small flows and ponds may have

457   cooled fairly quickly, before they had time to form smooth surfaces. In the case of larger

458   craters, like Tycho and Glushko, late stage injection of melt from draining ponds at higher

459   elevations may have broken up a previously frozen surface and created a very rugged and

460   broken terrain.

461   In some cases, particularly for rough radar-bright flows, the radar data often provides a

462   more useful view of flow margins than optical data, where the surface can be mantled by fine-

463   grained regolith. Young impact craters, such as Tycho, have relatively unburied melts that are

464   readily apparent in both radar and optical data. Many of the melt deposits and flows described

465   here are associated with craters that have ray systems and hence are geologically young. Over

466   time, the crater ejecta, including ray systems and ejecta flows, are destroyed and buried by

467   subsequent impacts.

468   *Ghent et al.* [2005] showed that younger craters often have radar-dark haloes in 70-cm

469   wavelength radar data, and that older craters do not have these haloes. These haloes have been

470   attributed to a layer of fine-grained ejecta mantling that becomes mixed into the underlying,

471   blocky ejecta blanket over time [*Ghent et al.* 2005]. Two of the features with impact melts

472   have radar dark haloes (Tycho and Aristillus), but the others discussed above are located on

473   the lunar limb or farside where no 70-cm wavelength radar data is currently available. There

474   is clearly a process by which ray systems, radar dark haloes, and ejecta flow features are

475   erased, but it is not yet clear what timeline this process follows or how it varies with crater

476 size. Future comprehensive searches of the radar data will help to improve the statistics of

477 which types and ages of craters have melt deposits and ejecta flows.

478   The combination of radar and optical data for the lunar impact melts also has some

479 implications for the surface textures of impact melt flows on Venus, for which only radar data

480 is available. In particular, as proposed by *Johnson and Baker* [1994], the lunar data suggest

481 that many of the changes in radar reflectivity within large complex melt flows are probably

482 due to flow features similar to those seen in terrestrial lava flows, such as ponding, rafted and

483 overturned plates, channeling, and pressure ridges. Some of the Venus flows appear darker to

484 the radar and have been interpreted as turbulent run-out flows that carry debris [*Schultz* 1992].

485 These Venus flows have some similar radar characteristics to the flows associated with

486 Jackson and the small crater near Maunder, which are darker to the radar and show no optical

487 evidence for flowing, melted rock. The impact process may sometimes produce debris flows

488 that are visible in radar images due to the sharp contrast in topography and roughness of the

489 emplaced material relative to the surroundings.

490

491 **4. Summary and Future Work**

492   Recent radar imaging data suggests that impact melt flows and ponds are more

493 common on the Moon than was previously known. The CPR values of the melt flows are

494 generally high and most of the flows have very rugged surfaces. Some lunar impacts cause

495 debris to be deposited in a flow-like manner, and these flows are often visible in radar images

496 due to their rough edges and topographic expression. Future work will aim to achieve better

497 statistics on the number and size of craters with melt flows and ponds. The Mini-RF data will

498 be useful for understanding the amount of melt produced by impacts, as well as the directions

499   in which most of the melt traveled. A systematic search of young and rayed crater systems

500   using high resolution radar imaging is likely to yield additional data on buried and partially

501   buried melt flows, including how the melt flows are buried and eroded over time.

502

509

510

510   **References**

511

512   Arvidson R., R. Drozd, E. Guiness, C. Hohenberg, C. Morgan, R. Morrison and V. Oberbeck

513   V (1976), Cosmic ray exposure age of Apollo 17 samples and the age of Tycho. *Proc. Lunar*

514   *Sci. Conf. 7*, 2817-2832.

515

516   Asimow, P. D. and J. A. Wood (1992), Fluid Outflows from Venus Impact Craters: Analysis

517   from Magellan Data, *J. Geophys Res., 97*, E8, 13643-13665.

518

519   Bray, V. J., L. L. Tornabene, L. P. Keszthelyi, A. S. McEwen, B. R. Hawke, T. A. Giguere, S.

520   A. Kattenhorn, W. B. Garry, B. Rizk, C. M. Caudill, L. R. Gaddis, and C. H. van der Bogert

521   (2010), New Insight into Lunar Impact Melt Mobility from the LRO Camera, *Geophys. Res.*

522   *Lett., 37*, L21202, doi:10.1029/2010GL044666.

523

524   Campbell, B. A. and D. B. Campbell (1992), Analysis of volcanic surface morphology on

525   Venus from comparison of Arecibo, Magellan, and terrestrial airborne radar data, *J. Geophys.*

526   *Res., 97 (E10)*, 16293-16314.

527

528   Campbell, B. A. (2009), Scale dependent surface roughness behavior and its impact on

529   empirical models for radar backscatter, *IEEE Trans. Geosci. Rem. Sens. 47*,

530   doi:10.1109/TGRS.2009.2022752, 3480-3488.

531

532   Campbell, B. A., L. M. Carter, D. B. Campbell, M. C. Nolan, J. F. Chandler, R. R. Ghent, B.

533   R. Hawke, R. F. Anderson and K. S. Wells (2010), Earth-Based S-band Radar Mapping of the

534   Moon: New Views of Impact Melt Distribution and Mare Physical Properties, *Icarus*, *208*,

535   doi:10.1016/j.icarus.2010.03.011.

536

537   Carrier, W. D., G. R. Ohloeft and W. Mendell (1991), Physical properties of the lunar surface,

538   in *Lunar Sourcebook*, 475-567, Cambridge Univ. Press, New York.

539

540   Carter, L. M., D. B. Campbell and B. A. Campbell (2011), Geologic studies of planetary

541   surfaces using radar polarimetric imaging, *Proc. IEEE, 99*,

542   doi:10.1109/JPROC.2010.2099090.

543

544   Chadwick, D. J. and G. G. Schaber (1993), Impact Crater Outflows on Venus: Morphology

545   and Emplacement Mechanisms, *J. Geophys. Res., 98*, 20891-20902.

546

547   Fink, J. H. and R. C. Fletcher (1978), Ropy Pahoehoe: Surface Folding of a Viscous Fluid, *J.*

548   *Volcan. Geothem. Res., 4*, 151-170.

549

550   Ghent, R. R., D. W. Leverington, B. A. Campbell, B. R. Hawke and D. B. Campbell (2005),

551   Earth-based observations of radar-dark crater haloes on the Moon: Implications for regolith

552   properties, *JGR*, *110*, E02005, doi:10.1029/ 2004JE002366.

553

554   Green, P. E (1968), Radar Measurements of Target Scattering Properties, in Radar

555   Astronomy, eds. J. V. Evans and T. Hagfors, McGraw-Hill, New York, New York.

556

557   Guest, J. E. (1973) Stratigraphy of ejecta from the lunar crater Aristarchus, *Geol. Soc.*

558   *America Bull., 84*, 2873-2894.

559

560   Hawke, B. R. and J. W. Head (1977), Impact melt on lunar crater rims, in Impact and

561   Explosion Cratering, eds. D. J. Roddy, R. O. Pepin and R. B. Merrill, Pergamon Press, New

562   York, pp. 815-841.

563

564   Howard, K. A. and H. G. Wilshire (1975), Flows of impact melt at lunar craters, *J. Res. U. S.*

565   *Geol. Survey, 3*, no. 2, 237-251.

566

567   Jackson, J. D. (1999), Classical Electrodynamics, Third Edition, John Wiley and Sons, New

568   York, New York.

569

570   Johnson, J. R. and V. R. Baker (1994), Surface Property Variations in Venusian Fluidized

571   Ejecta Blanket Craters, *Icarus, 110*, 33-70.

572

573   Phillips, R. J., R. E. Arvidson, J. M. Boyce, D. B. Campbell, J. E. Guest, G. G. Schaber and L.

574   A. Soderblom (1991), Impact Craters on Venus: Initial Analysis from Magellan, *Science, 252*,

575   288-296

576

577   Pierazzo, E. and H. J. Melosh (2000), Melt Production in Oblique Impacts, *Icarus, 145*, 252-

578   261.

579

580   Raney, R. K., P. D. Spudis,   B. Bussey, J. Crusan, J. R. Jensen, W. Marinelli,

581   P. McKerracher, C. Neish, M. Palsetia, R. Schulze, H. B. Sequeira, and H. Winters (2011),

582   The Lunar Mini-RF Radars: Hybrid Polarimetric Architecture and Initial Results, *Proc IEEE,*

583   *99,* doi: 10.1109/JPROC.2010.2084970, 808-823.

584

585   Robinson, M. S., and 22 coauthors (2010), Lunar Reconnaissance Orbiter Camera (LROC)

586   instrument overview, *Space Sci. Rev., 150,* 81–124, doi:10.1007/s11214-010- 9634-2.

587

588   Robinson, M. S., P.C. Thomas, B. W. Denevi, T. Tran, E. B. Cisneros, J. Plescia, C. H. van

589   der Bogert, and H. Hiesinger (2011), Highland Plains, an Exceptional Grouping, 42nd Lunar

590   Plan. Sci. Conf., abstract #2511.

591

592   Ryder G., D. Bogard and D. Garrison (1991), Probable age of Autolycus and calibration of

593   lunar stratigraphy, *Geology, 19,* 143-146.

594

595   Schultz, P. H. (1992) Atmospheric Effects on Ejecta Emplacement and Crater Formation on

596   Venus from Magellan, *J. Geophys. Res., 97,* E10, 16183-16248.

597

598   Schultz, P. H. (1996), Effect of impact angle on vaporization, *J. Geophys. Res., 101,* E9,

599   21117-21136.

600

601   Shoemaker E.M., R. M. Batson, H. E. Hole, E. C. Morris, J. J. Rennilson and E. A. Whitaker

602   (1968), Television observations from Surveyor VII. In Surveyor VII: A Preliminary Report,

603   *NASA SP-173*, 13-81.

604

605   Stacy, N. J. S. (1993), High resolution synthetic aperture radar observations of the Moon, PhD

606   dissertation, Dept. of Astronomy, Cornell University.

607

608   Theilig, E. and R. Greeley (1986), Lava Flows on Mars: Analysis of Small Surface Features

609   and Comparisons with Terrestrial Analogs, *J. Geophys. Res., 91*, B13, E193-E206.

610

611   Ulaby, F. T., R. K. Moore, and A. K. Fung (1986), Microwave Remote Sensing: Active and

612   Passive, Volume 2, Artech House, Norwood, Massachusetts.

613

613 **Figures:**

614

615 **Figure 1:** Mini-RF images of impact melt deposits to the east of Tycho. (a) A total power

616 radar backscatter image. Radar illumination is from the left. (b) A CPR image stretched to a

617 color scale and overlaid on the total power image. The Tycho ejecta deposits have very high

618 CPR values, but the values are particularly large in radar-bright areas that correspond to very

619 rugged impact melt flows. The positions of Fig. 2b and 2c are marked on (a).

620

621 **Figure 2:** Surface textures associated with different radar backscatter characteristics. (a)

622 High-resolution images from LROC NAC (M116372249) show highly disrupted terrain that

623 corresponds to CPR values greater than one. The roughest areas have ridges, mounds, and

624 upturned plates. (b) An LROC NAC image (M119916367) showing rafted plates. These areas

625 also have elevated CPR values, although the values remain below one. (c) A Kaguya Terrain

626 Camera image showing a section of the southern melt flow and pond. The position of Fig 2a

627 is marked with a white box. The outline of an area of pressure ridges within the pond is

628 marked with arrows. This may represent late stage flow into the pond; alternatively, the pond

629 may have formed via a breakout from an initially smaller flow. Parts (b) and (c) are marked

630 on the radar image in Figure 1.

631

632 **Figure 3:** Four images of the impact melt flows northeast of Aristillus. (a) A context image

633 from the LROC WAC mosaic. (b) Mini-RF total power image; radar illumination is from the

634 right. The radar-bright impact melts are mostly connected, but some isolated ponds are

635 present. (c) Mini-RF CPR image, stretched to a color scale and overlaid on the total power

636   image. The impact melts have higher CPR values than the surrounding terrain, but they are

637   less than what is measured for Tycho. The gradient across the image is due to the calibration

638   errors discussed in section 2. (d) Kaguya Terrain Camera image of the same area. The melt

639   flows are barely visible and have been smoothed over by a regolith coating.

640

641   **Figure 4:** Flow features east of Jackson crater. (a) An LROC WAC context image showing

642   the location of the radar data. (b) Radar total power images (left and right sides) overlaid on

643   the WAC image. Radar illumination is from the right. Arrows mark the positions of flow-like

644   features. Although the features are somewhat brighter than their surroundings, they are not as

645   bright and well-defined as the Tycho and Aristillus melt flows. (c) CPR image of the western

646   (left) radar image in (b), generated by stretching the CPR data to a color scale and overlaying

647   on the total power image. (d) A CPR overlay of the eastern (right) radar image in (b). Parts of

648   the flow features have CPR values that are slightly elevated compared to nearby terrain, but

649   the CPR values are not distinctly different from the proximal ejecta, as is seen at Tycho and

650   Aristillus. Optical images show no evidence of ponded melt. These features may be generated

651   by debris flows.

652

653   **Figure 5:** Flows north of the crater Glushko. (a) Mini-RF total power image. Radar

654   illumination is from the right. The location of the image in part C is shown with a box. (b)

655   CPR image stretched to a color scale and overlaid on the total power image. (c) An LROC

656   NAC image of part of the Gluskho flows. As with Tycho, radar-bright, high CPR parts of the

657   flow have rugged flow features, such as pressure ridges. The flow features are not pronounced

658   as they are for Tycho, and the surface may have a thicker mantling layer.

659

Figure 6: Impact melt flows west of the crater Gerasimovich D. (a) An LROC Wide-Angle

Camera image of the crater and surrounding area. The impact melt flows are visible in some

places, but are generally covered by regolith. (b) Mini-RF total backscatter power images.

Radar illumination is from the left. The radar wave penetrates through thin regolith cover to

reveal the flow outlines. The flow has a fairly uniform radar brightness compared to the

Tycho and Glushko flows, but there are subtle brightness changes that may indicate smoother

and rougher parts of the buried flow or variations in regolith depth.

667

Figure 7: The Wiener F flow and pond. (a) High-resolution Lunar Orbiter images (LO5-

103H2 and H3) have a lighting geometry that highlights the structure of the melt pond. The

pond has rough ridges on the surface. North is to the right in this image. Arrows highlight the

same features in both images: the edge of the melt pond and a flow feature higher on the rim.

(b) Mini-RF total power image of the pond. North is to the right, and the radar illumination is

from the top. The flow feature on the crater wall is particularly apparent in the radar data.

674

Figure 8: Mini-RF images of a pond associated with a small (13.5 km), unnamed crater

(30.9° S, 145.5° E). (a) The total power backscatter radar image. Radar illumination is from

the left, and the position of image part C is shown with a box. (b) The circular polarization

ratio, stretched to a color scale and overlaid on the total power image. The pond is radar-

bright with high CPR values. (c) Total power image of the small pond, which is cratered.

680

681   **Figure 9:** An unnamed 13-km diameter crater (35.7° N, 166.0° E) with an unusual radar-dark

682   lane on top of a possible melt flow or veneer. (a) The radar total power image; illumination is

683   from the left. The location of the Kaguya image in part c is marked with a box. (b) The

684   circular polarization ratio image stretched to a color scale and overlaid on the total power

685   image. (c) A Kaguya image of part of the impact melt and radar-dark region. There is no

686   obvious surface expression of the radar-dark lane. Arrows in (a) and (b) mark the location of a

687   thin outshoot of the dark lane that has rounded edges suggestive of some type of flow.

688

689   **Figure 10:** Images of flow features associated with a small (5 km diameter) crater northeast

690   of Maunder crater in the Orientale basin. North is towards the top of the images. (a) A radar

691   total-power image mosaic; illumination is from the left. The location of the images in parts b

692   and c are marked with boxes. Arrows mark the location of flow-like features distant from the

693   central crater. (b) A Kaguya Terrain Camera image of a flow feature northwest of the crater.

694   The feature corresponds to an area of bright debris that appears to have flowed downhill into a

695   valley. (c) A Kaguya Terrain Camera image of radar-bright crater ejecta that has been

696   deposited along the rim of Maunder crater.

697

698   **Figure 11:** Images of ponds and flows near Keeler crater. Most of the melt is north of the

699   crater Keeler S. (a) A LROC WAC context image with craters labeled. A box marks the

700   locations of parts b and d. (b) A Kaguya Terrain Camera image of the area of ponds. Some of

701   the more easily visible ponds are marked with arrows. An arrow also marks the location of a

702   small pond and flow that is easily visible in the radar data. A box marks the area covered by

703   the close-up images in Figure 12. (c) A circular polarization ratio image of part of the melt

704 pond field. This image corresponds to the left-most radar image in part d. The location of the

705 small pond and flow is marked. Most of the ponds have CPR values between 0.6 and 0.7,

706 suggesting that they are rougher than their surroundings, but probably partially buried. (d)

707 Radar total backscatter images of the area shown in part b. The backscatter images show

708 multiple radar-bright ponds and flow features, including flows into Keeler V. Radar

709 illumination is from the left.

710

711 **Figure 12:** A close-up view of Keeler-area melt ponds and flows. The image location is

712 marked in Figure 11. (a) Kaguya image with ponds marked. (b) Corresponding total power

713 radar image. Note that in the optical image, the illumination is from the right but in the radar

714 image, the illumination is from the left. Arrows mark the position of ponded material at the

715 bottom of a hill. The radar image shows a radar bright streak that could be melt material that

716 flowed down the side of the hill. On the right side of the optical image, there is a pond that

717 does not appear to show up in the radar data, probably because the radar viewing geometry

718 shifts the bottom of the crater off the edge of the image. An additional, barely visible, pond is

719 visible in the lower right of the image. Arrows mark the pond and a slightly flat sinuous ridge

720 leading down to the pond.

721

722 **Figure 13:** Mini-RF images of the pond field located at 41° N and 166° E [*Robinson et al.*

723 2011]. (a) Total backscatter power. (b) Circular polarization ratio image stretched to a color

724 scale and overlaid on the total power image. The ponds at this site have higher CPR values

725 than the ponds at Keeler, but they also appear to be less buried in both radar and optical

726 imagery [*Robinson et al.* 2011]. Radar illumination is from the left.

727

Figure 1: Mini-RF images of impact melt deposits to the east of Tycho. (a) A total power radar backscatter image. Radar illumination is from the left. (b) A CPR image stretched to a color scale and overlaid on the total power image. The Tycho ejecta deposits have very high CPR values, but the values are particularly large in radar-bright areas that correspond to very rugged impact melt flows. The positions of Fig. 2b and 2c are marked on (a).
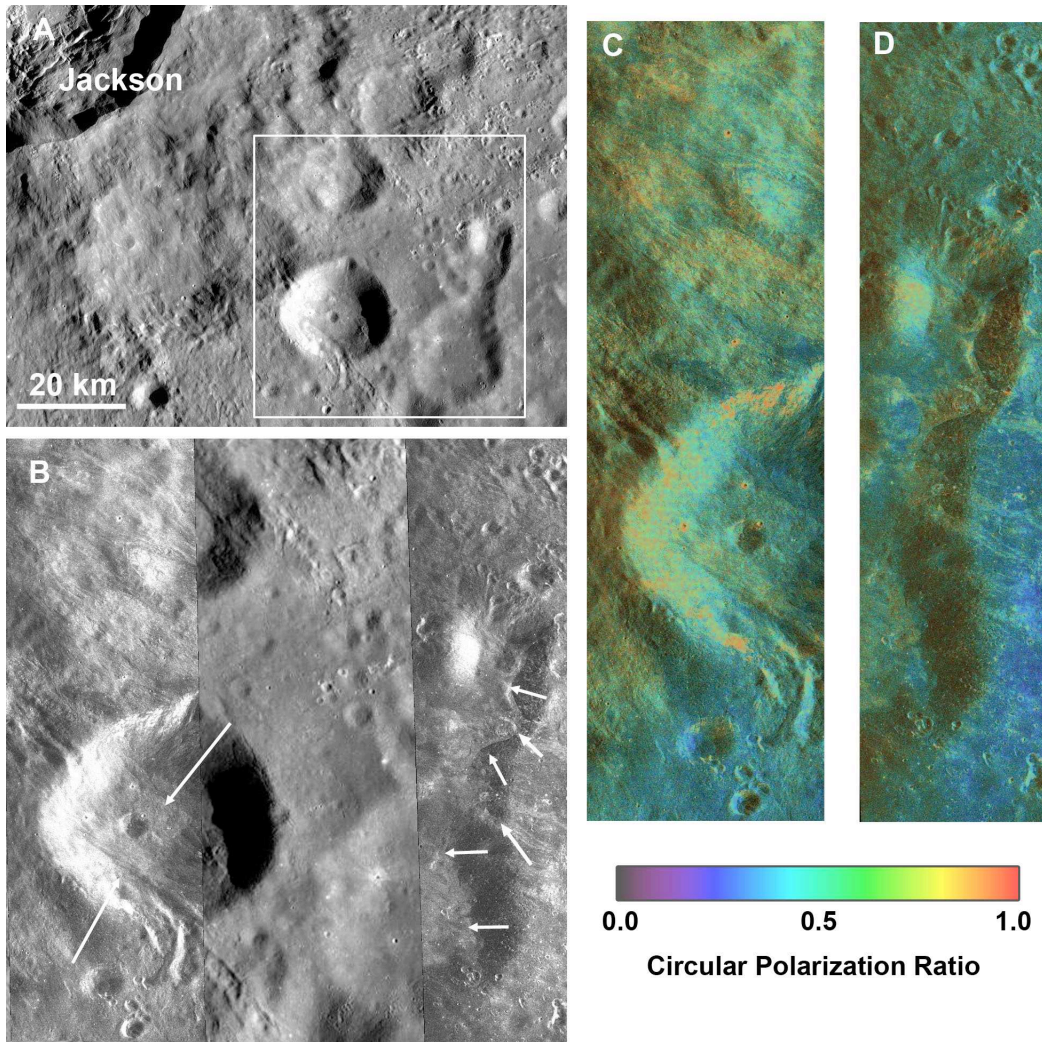
735 **Figure 2:** Surface textures associated with different radar backscatter characteristics. (a)
736 High-resolution images from LROC NAC (M116372249) show highly disrupted terrain that
737 corresponds to CPR values greater than one. The roughest areas have ridges, mounds, and
738 upturned plates. (b) An LROC NAC image (M119916367) showing rafted plates. These areas
739 also have elevated CPR values, although the values remain below one. (c) A Kaguya Terrain
740 Camera image showing a section of the southern melt flow and pond. The position of Fig 2a
741 is marked with a white box. The outline of an area of pressure ridges within the pond is
742 marked with arrows. This may represent late stage flow into the pond; alternatively, the pond
743 may have formed via a breakout from an initially smaller flow. Parts (b) and (c) are marked
744 on the radar image in Figure 1.
745

745

746

Figure 3: Four images of the impact melt flows northeast of Aristillus. (a) A context image
from the LROC WAC mosaic. (b) Mini-RF total power image; radar illumination is from the
right. The radar-bright impact melts are mostly connected, but some isolated ponds are
present. (c) Mini-RF CPR image, stretched to a color scale and overlaid on the total power
image. The impact melts have higher CPR values than the surrounding terrain, but they are
less than what is measured for Tycho. The gradient across the image is due to the calibration
errors discussed in section 2. (d) Kaguya Terrain Camera image of the same area. The melt
flows are barely visible and have been smoothed over by a regolith coating.

Figure 4: Flow features east of Jackson crater. (a) An LROC WAC context image showing the location of the radar data. (b) Radar total power images (left and right sides) overlaid on the WAC image. Radar illumination is from the right. Arrows mark the positions of flow-like features. Although the features are somewhat brighter than their surroundings, they are not as bright and well-defined as the Tycho and Aristillus melt flows. (c) CPR image of the western (left) radar image in (b), generated by stretching the CPR data to a color scale and overlaying on the total power image. (d) A CPR overlay of the eastern (right) radar image in (b). Parts of the flow features have CPR values that are slightly elevated compared to nearby terrain, but the CPR values are not distinctly different from the proximal ejecta, as is seen at Tycho and Aristillus. Optical images show no evidence of ponded melt. These features may be generated by debris flows.

Figure 5: Flows north of the crater Glushko. (a) Mini-RF total power image. Radar illumination is from the right. The location of the image in part C is shown with a box. (b) CPR image stretched to a color scale and overlaid on the total power image. (c) An LROC NAC image of part of the Gluskho flows. As with Tycho, radar-bright, high CPR parts of the flow have rugged flow features, such as pressure ridges. The flow features are not pronounced as they are for Tycho, and the surface may have a thicker mantling layer.

776

777

Figure 6: Impact melt flows west of the crater Gerasimovich D. (a) An LROC Wide-Angle
Camera image of the crater and surrounding area. The impact melt flows are visible in some
places, but are generally covered by regolith. (b) Mini-RF total backscatter power images.
Radar illumination is from the left. The radar wave penetrates through thin regolith cover to
reveal the flow outlines. The flow has a fairly uniform radar brightness compared to the
Tycho and Glushko flows, but there are subtle brightness changes that may indicate smoother
and rougher parts of the buried flow or variations in regolith depth.

785

785

786
787 **Figure 7**: The Wiener F flow and pond. (a) High-resolution Lunar Orbiter images (LO5-
788 103H2 and H3) have a lighting geometry that highlights the structure of the melt pond. The
789 pond has rough ridges on the surface. North is to the right in this image. Arrows highlight the
790 same features in both images: the edge of the melt pond and a flow feature higher on the rim.
791 (b) Mini-RF total power image of the pond. North is to the right, and the radar illumination is
792 from the top. The flow feature on the crater wall is particularly apparent in the radar data.
793
794

795

Figure 8: Mini-RF images of a pond associated with a small (13.5 km), unnamed crater (30.9° S, 145.5° E). (a) The total power backscatter radar image. Radar illumination is from the left, and the position of image part C is shown with a box. (b) The circular polarization ratio, stretched to a color scale and overlaid on the total power image. The pond is radar-bright with high CPR values. (c) Total power image of the small pond, which is cratered.

803

Figure 9: An unnamed 13-km diameter crater (35.7° N, 166.0° E) with an unusual radar-dark lane on top of a possible melt flow or veneer. (a) The radar total power image; illumination is from the left. The location of the Kaguya image in part c is marked with a box. (b) The circular polarization ratio image stretched to a color scale and overlaid on the total power image. (c) A Kaguya image of part of the impact melt and radar-dark region. There is no obvious surface expression of the radar-dark lane. Arrows in (a) and (b) mark the location of a thin outshoot of the dark lane that has rounded edges suggestive of some type of flow.

811

811

812

813 **Figure 10:** Images of flow features associated with a small (5 km diameter) crater northeast
814 of Maunder crater in the Orientale basin. North is towards the top of the images. (a) A radar
815 total-power image mosaic; illumination is from the left. The location of the images in parts b
816 and c are marked with boxes. Arrows mark the location of flow-like features distant from the
817 central crater. (b) A Kaguya Terrain Camera image of a flow feature northwest of the crater.
818 The feature corresponds to an area of bright debris that appears to have flowed downhill into a
819 valley. (c) A Kaguya Terrain Camera image of radar-bright crater ejecta that has been
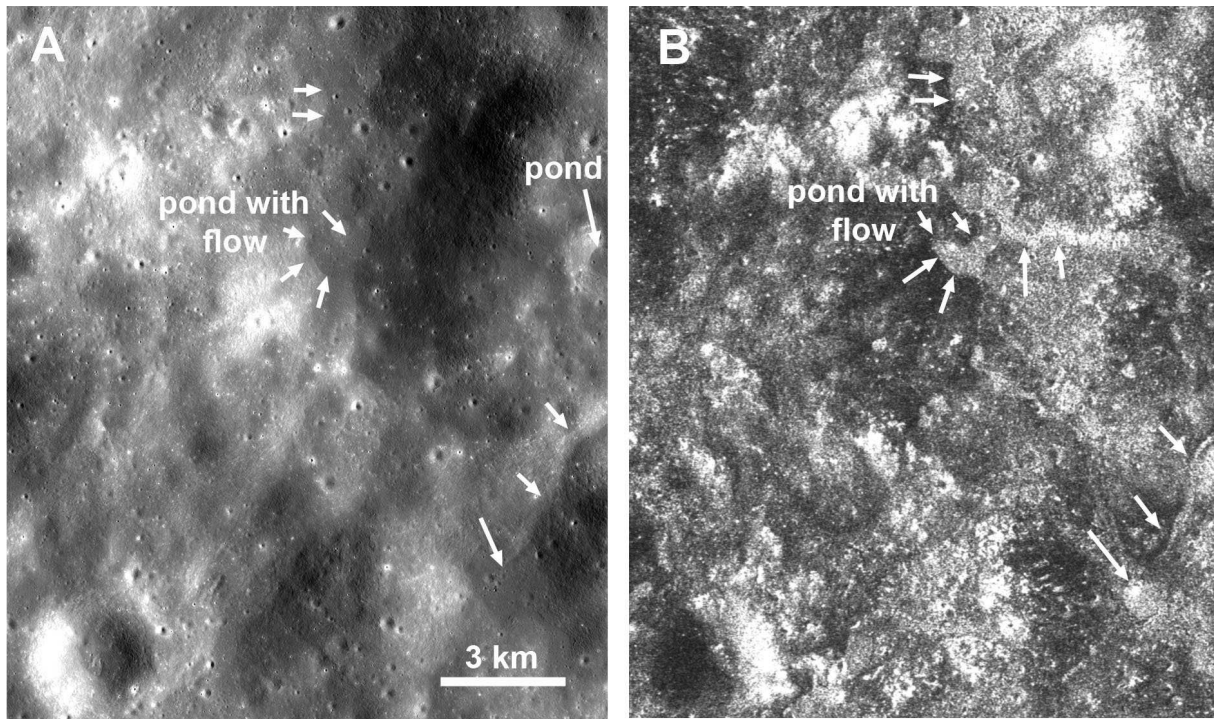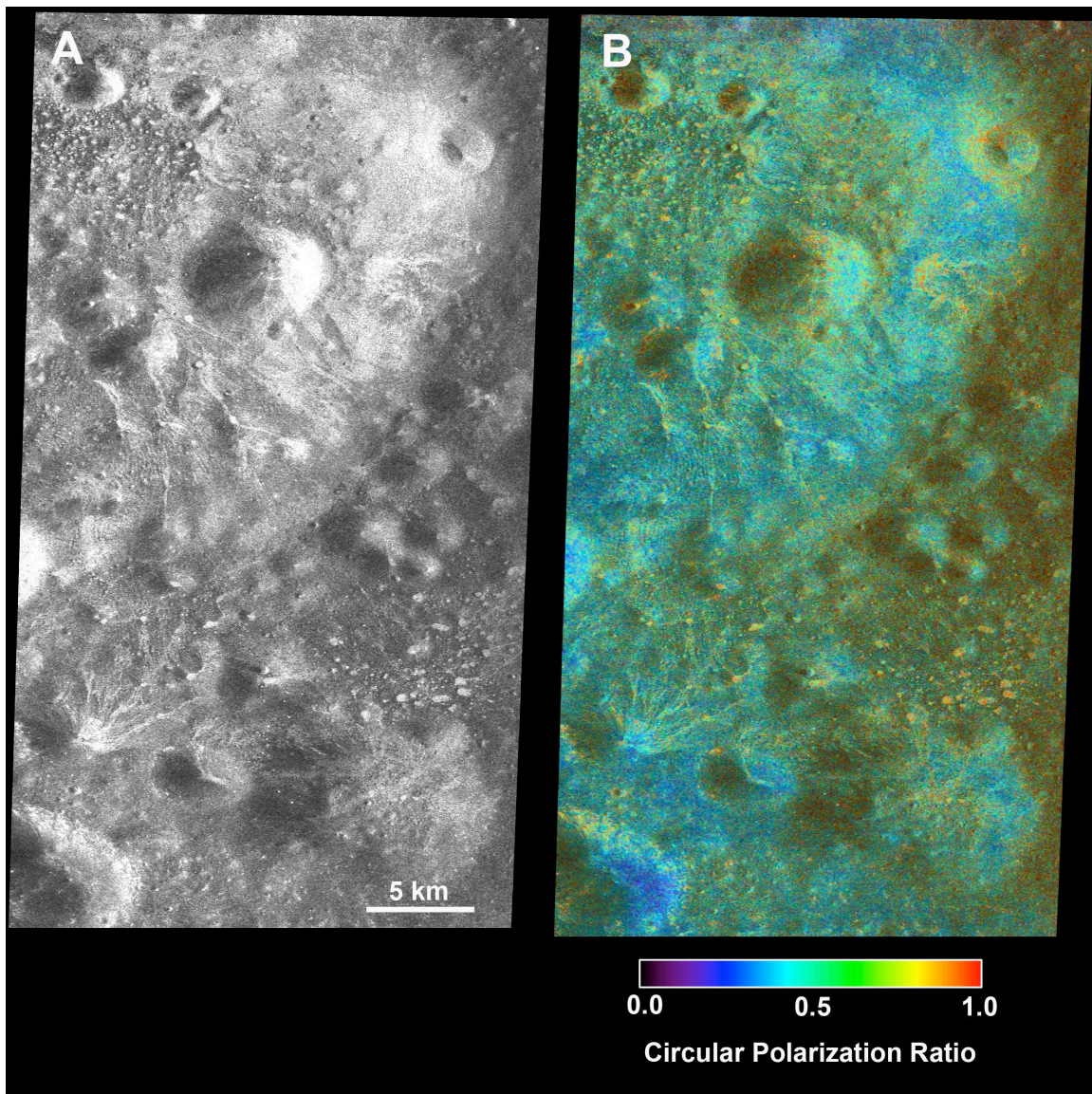820 deposited along the rim of Maunder crater.
821
822
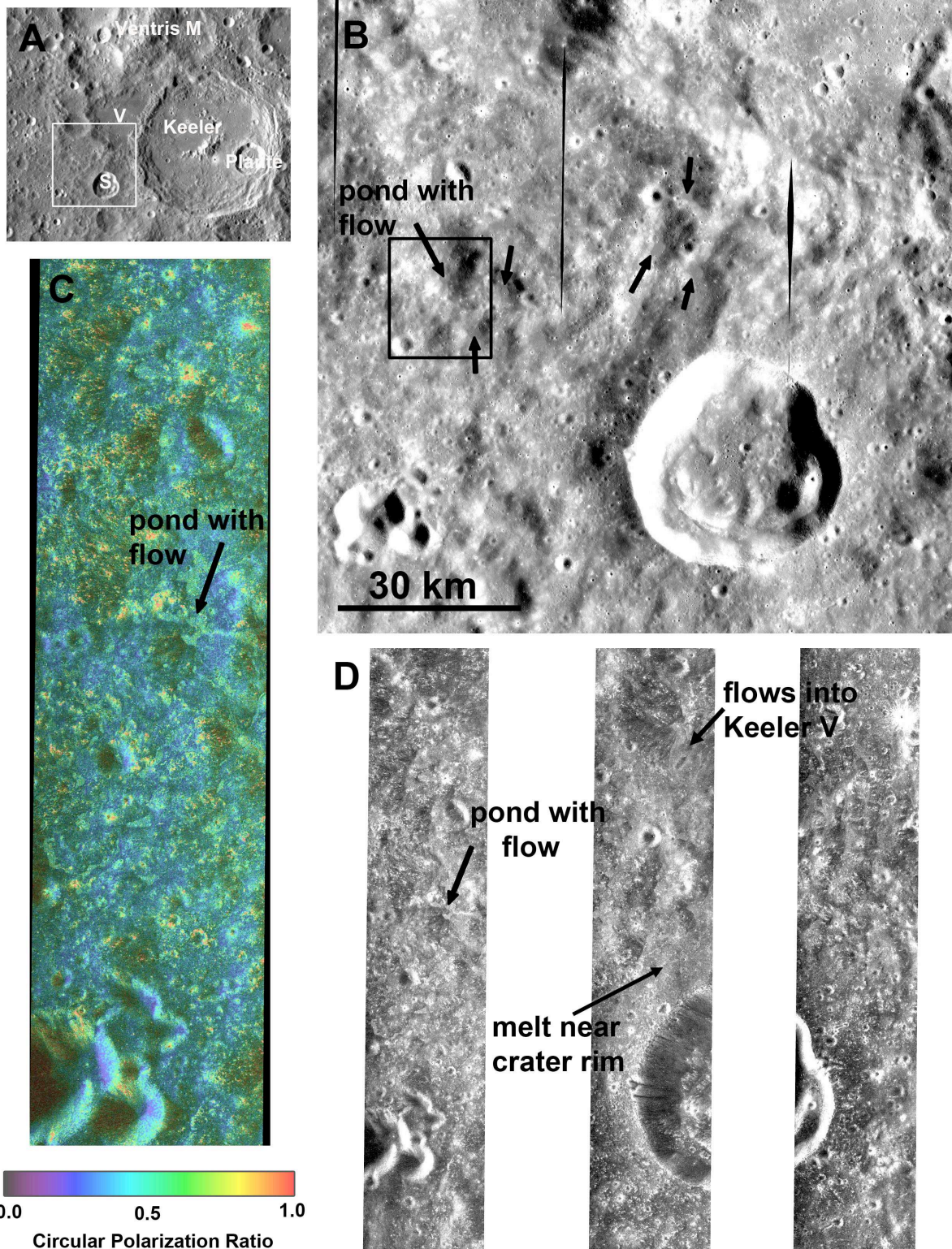
Figure 11: Images of ponds and flows near Keeler crater. Most of the melt is north of the crater Keeler S. (a) A LROC WAC context image with craters labeled. A box marks the locations of parts b and d. (b) A Kaguya Terrain Camera image of the area of ponds. Some of

826   the more easily visible ponds are marked with arrows. An arrow also marks the location of a

827   small pond and flow that is easily visible in the radar data. A box marks the area covered by

828   the close-up images in Figure 12. (c) A circular polarization ratio image of part of the melt

829   pond field. This image corresponds to the left-most radar image in part d. The location of the

830   small pond and flow is marked. Most of the ponds have CPR values between 0.6 and 0.7,

831   suggesting that they are rougher than their surroundings, but probably partially buried. (d)

832   Radar total backscatter images of the area shown in part b. The backscatter images show

833   multiple radar-bright ponds and flow features, including flows into Keeler V. Radar

834   illumination is from the left.

835

835
836

Figure 12: A close-up view of Keeler-area melt ponds and flows. The image location is
marked in Figure 11. (a) Kaguya image with ponds marked. (b) Corresponding total power
radar image. Note that in the optical image, the illumination is from the right but in the radar
image, the illumination is from the left. Arrows mark the position of ponded material at the
bottom of a hill. The radar image shows a radar bright streak that could be melt material that
flowed down the side of the hill. On the right side of the optical image, there is a pond that
does not appear to show up in the radar data, probably because the radar viewing geometry
shifts the bottom of the crater off the edge of the image. An additional, barely visible, pond is
visible in the lower right of the image. Arrows mark the pond and a slightly flat sinuous ridge
leading down to the pond.

Figure 13: Mini-RF images of the pond field located at 41° N and 166° E [*Robinson et al.* 2011]. (a) Total backscatter power. (b) Circular polarization ratio image stretched to a color scale and overlaid on the total power image. The ponds at this site have higher CPR values than the ponds at Keeler, but they also appear to be less buried in both radar and optical imagery [*Robinson et al.* 2011]. Radar illumination is from the left.